2012

Electrical impedance-based void fraction measurement and flow regime identification in microchannel flows under adiabatic conditions

Sidharth Paranjape
Purdue University

Susan N. Ritchey
Purdue University

S V. Garimella
Purdue University, sureshg@purdue.edu

Paranjape, Sidharth; Ritchey, Susan N.; and Garimella, S V., "Electrical impedance-based void fraction measurement and flow regime identification in microchannel flows under adiabatic conditions" (2012). *CTRC Research Publications.* Paper 167.
http://dx.doi.org/10.1016/j.ijmultiphaseflow.2012.02.010

ELECTRICAL IMPEDANCE-BASED VOID FRACTION MEASUREMENT AND FLOW REGIME IDENTIFICATION IN MICROCHANNEL FLOWS UNDER ADIABATIC CONDITIONS

Sidharth Paranjape, Susan N. Ritchey, and Suresh V. Garimella*

Cooling Technologies Research Center, an NSF I/UCRC

School of Mechanical Engineering

Purdue University

West Lafayette, IN 47907 USA

*Corresponding author: Tel: 1-765- 494-5621, Email: sureshg@purdue.edu

Abstract

Electrical impedance of a two-phase mixture is a function of void fraction and phase distribution. The difference in the specific electrical conductance and permittivity of the two phases is exploited to measure electrical impedance for obtaining void fraction and flow regime characteristics. An electrical impedance meter is constructed for the measurement of void fraction in microchannel two-phase flow. The experiments are conducted in air-water two-phase flow under adiabatic conditions. A transparent acrylic test section of hydraulic diameter 780 μm is used in the experimental investigation. The impedance void meter is calibrated against the void fraction calculated using analysis of images obtained with a high-speed camera. Based on these measurements, a methodology utilizing the statistical characteristics of the void fraction signals is employed for identification of microchannel flow regimes. A self-organizing neural network is used for classification of the flow regimes.

Keywords: Microchannel flow, two-phase flow, void fraction, impedance meter, flow regimes

1. Introduction

Microchannel heat sinks based on boiling and two-phase flow can meet the increasing cooling needs for high-end electronics systems in applications ranging from high-performance computers to avionics and spacecraft to electric vehicles. In order to design and build such heat sinks, a unified model accounting for the prevalent flow regimes is needed to predict the boiling heat transfer rates and pressure drops in microchannels. Flow regime-based correlations are desired in two-phase flow analyses since a single heat transfer correlation does not apply in all flow regimes (Hewitt, 1983). A number of studies in recent years have attempted to better understand the flow patterns during boiling in microchannels using various working fluids as reviewed in Sobhan and Garimella (2001), Garimella and Sobhan (2003) and Bertsch et al. (2008). A systematic investigation into the effects of channel size, mass flux and heat flux on the boiling flow patterns and heat transfer in microchannels was recently performed by Harirchian and Garimella (2008, 2009). A generalized flow regime map for boiling in microchannels covering a wide range of channel geometries, heat fluxes and mass fluxes was developed in terms of three non-dimensional parameters – Boiling number, Reynolds number and Bond number – by Harirchian and Garimella (2010).

In order to further develop predictive models for flow regime transitions, it is necessary to measure void fraction in two-phase flow, since void fraction and its temporal variation is a characteristic of the flow regime. Several studies in the past have relied on flow visualization for the identification of flow regimes as well as for the measurement of void fraction (Serizawa et al., 2002, Kawahara et al., 2006, Kawaji et al., 2006, and Kawahara et al., 2009). Though flow regimes can be determined by observing high-speed movie camera recordings, the method is subjective and cannot be used for conditions in which intermittent phenomena occur, as well as

when the aspect ratios of the observed field is such that the mechanisms are obscured from visual observation. In order to overcome these shortcomings, a non-intrusive void fraction measurement technique, which is based on the measurement of electrical impedance, is explored in the present study. Electrical impedance-based void fraction measurements have been successfully performed in the past several decades in macroscale two-phase flows. For cross-sectional area-averaged or volume-averaged measurements, impedance void meters with electrodes flush mounted to the channel walls were used by Asali et al. (1985), Andreussi et al. (1988), Tsochatzidis et al. (1992), Fossa (1998) and Mi et al. (1998). A theoretical basis for this design is given in Coney (1973). A similar geometry of the impedance meter is adapted to the microscale channels considered in the present study. The practical implementation of the electronic circuit measures the net electrical admittance, *i.e.*, the inverse of electrical impedance, of the two-phase mixture. The admittance is a function of the material properties (specific conductance and electrical permittivity of the two phases), the void fraction and the flow regime. The specific conductance determines the conductive reactance, while the permittivity determines the capacitive reactance. For a given geometry of electrodes, an appropriately normalized admittance is a function of void fraction and flow regime.

Two-phase flow regimes are typically described using qualitative categorization of flow visualizations. This involves subjectivity in their identification. In order to overcome this difficulty, Jones and Zuber (1975) first employed quantitative means for flow regime determination. Using an X-ray source, they measured the temporal variation of the area-averaged void fraction in a rectangular channel (10 cm × 1 cm) and plotted a probability density function (PDF) of the void fraction. The significant differences in the PDF between various flow regimes suggested their use for flow regime determination. Later studies by Tutu (1982) and

Matsui (1984) used void fraction distributions obtained with differential pressure transducers, while non-intrusive impedance void meters were used by Mi et al. (1998) as flow regime indicators. A comprehensive study by Costigan and Whalley (1997) on flow regimes in vertical upflow used segmental impedance electrodes to determine void fraction, combined with the PDF technique. Recently, bubble chord-length distributions obtained from conductivity probes were used as flow regime indicators by Julia et al. (2008). The quantitative flow regime classification proposed by Mi et al. (1998) is adapted in the present study to identify the flow regimes.

The present work aims to develop an impedance-based void fraction sensor for microchannel two-phase flows. The experiments are conducted in air-water two-phase flow under adiabatic conditions. Flow regimes are identified quantitatively using the statistics of the signals acquired by the void fraction sensor.

2. Experimental method

2.1 Test section

An experimental test cell for void fraction measurements in air-water two-phase flow is fabricated in clear transparent acrylic to allow for visual observation. Figure 1 presents a photograph and drawing of the test setup. A flow channel with a 0.780 mm × 0.780 mm square cross-section is cut into the base plate. The length of the channel is 50.8 mm. Two 304 stainless steel electrodes are embedded in the base plate such that the faces of the electrodes are flush-mounted to the side walls of the channel. The electrodes are located 25.4 mm (32.6 hydraulic diameters) from the inlet of the microchannel. In this design, the width and height of the electrode faces are identical to the width and height of the flow channel, i.e., 0.780 mm. Inlet and outlet plenums are machined into the top cover plate to provide manifolds for water flow in

the flow channel. The top cover plate is equipped with tube fittings to connect the test cell to the flow loop. Single-phase water enters the flow channel from the inlet manifold. Air is directly injected into the flow channel through a 0.3 mm diameter orifice at the bottom of the flow channel. The air inlet orifice is located 10 mm downstream from the inlet of the flow channel. The electrodes are connected to the electronic circuit via 14 gauge copper cables. Silver epoxy is used to minimize the contact resistance between the electrodes and copper cables.

A flow loop is constructed to provide air and water flow through the test cell as shown in Figure 2. De-ionized water is used for the liquid stream. A small amount of morpholine and ammonium-hydroxide (1 mg of each per liter of de-ionized water) is added to the water in order to increase its electrical conductivity while keeping its pH value near 7. The impact of the addition of these chemicals on flow regimes, through a change in surface tension, is negligible as suggested by the study of Mi et al. (1998). The specific conductance of water is thus maintained at 100 μSiemens/cm. The water flow loop is equipped with a frequency-controlled water pump and a needle valve to control the water flow rate. The water flow rate is measured with a micro-turbine flow meter (McMillan Flo-106) with a range of 0 to 200 ml/min. Air flow is provided by a compressed air cylinder equipped with a pressure regulator. An air mass flow sensor (Omega FMA6704) with a range of 0 to 100 ml/min is used to measure the air flow rate through the test cell. The flow sensor also measures the temperature and pressure of the gas at the flow meter. The measured temperature and pressure are used to correct the mass flow rate from the standard conditions since the flow sensor is factory-calibrated at standard temperature and pressure. The air flow rate is controlled by a needle valve. Pressure is measured at the inlet and the outlet of the channel. The local pressure at the measurement point in the channel is interpolated based on these measurements. The actual volumetric flux of air is corrected for the interpolated pressure

at the measurement location. The storage tank is open to the atmosphere and also serves as an air-water flow separator. Special care is taken to avoid flow instabilities from occurring due to the accumulation of air in various tube fittings in the exit section of the flow loop. In order to achieve this, flexible tygon tubing is used to connect the exit of the test section to the storage tank, which is located at a higher elevation than the test section.

2.2 Impedance meter

An auto-balancing bridge method is implemented in a custom-built unit for measurement of the electrical impedance of the two-phase mixture in the test cell. Details of auto-balancing bridge methods are available in Tumanski (2006). The signal processing scheme is depicted in Figure 3. The test cell is excited with an alternating sine wave voltage signal with a peak-to-peak voltage difference of 3 V. The exciter signal is set at a frequency of 20 kHz. A current-to-voltage amplifier is used for measurement of the resulting current. The voltage measured across the reference resistor of the amplifier circuit serves as a measure of the current flowing through the test cell. This signal is referred to as the modulated signal, while the exciter signal is taken as the carrier wave. Both of these voltage signals are logged to a high-speed data acquisition system (National Instruments NI 6259-USB) at a sampling rate of 500 kHz. The data acquisition system has a 16-bit quantization for analog to digital conversion in the voltage range of -5 V to +5 V. The signals are then processed numerically using a MATLAB program developed in-house. The acquired signal is synchronously demodulated using the excitation signal and a 90º phase-shifted excitation signal in order to calculate the real and imaginary parts of the impedance. A low-pass Butterworth filter with cut-off frequency of 10 kHz is used to filter out

the excitation signal. The filtered signal is proportional to the electrical impedance of the two-phase mixture between the electrodes.

2.3 Image processing

A high-speed digital video camera (Photron Fastcam-Ultima APX) along with a Keyence VH-Z50L lens at 100X magnification is employed for flow visualization. The videos are acquired at 24,000 frames per second with a shutter speed of 120,000 Hz. An illumination source (Henke-Sass Wolf) is used to illuminate the microchannels for visualization. This combination provides a spatial resolution of 8 μm per pixel. The digital videos are acquired for 4 seconds for each flow condition. The stored images are further processed in order to calculate the void fraction. The image processing is performed in the sequence described below.

1. Rotate and crop each frame of the video to obtain a square-shaped interrogation window having the same width as that of the flow channel.
2. Remove the background and threshold the gray-scale image to obtain a binary image.
3. Detect edges of bubbles in the image using the Canny algorithm implemented in MATLAB (Mathworks Inc., 2009).
4. Remove unphysical boundaries detected due to reflection of light from bubble surfaces. This is achieved by algorithms implemented in MATLAB. The details of the algorithm are explained in Soille (2003).
5. Remove cusps and concave boundaries using the convex hull algorithm implemented in MATLAB.
6. Calculate the volumes and cross-sectional areas of bubbles and hence the volumetric void fraction and cross-sectional area-averaged void fractions, respectively. In order to calculate the bubble volume from two-dimensional information obtained by flow visualization, the

bubbles are assumed to be axisymmetric about their major axes. The uncertainties in the volume measurement made under this assumption need careful quantification, which is the focus of ongoing work. An approximate uncertainty analysis was performed for the calculation of bubble volume for the simple geometries of spherical and cylindrical bubbles. The maximum error was found to be 8% of the measured value.

7. Repeat Steps 1 through 6 for each frame in the movie to obtain a time series of the void fraction. Further, calculate a time average of the volume- and area-averaged void fractions for each flow condition.

Figure 4 illustrates the morphological operations performed in steps 1 through 5, which are used to extract the boundaries of the bubbles from the original image. The time-averaged void fractions calculated from the image processing of the videos are used as reference measurements to calibrate the impedance void meter.

2.4 Uncertainty analysis

The uncertainties in the measurements of the steady-state values of gas and liquid flow rates stem from a combination of uncertainty in the measurement by the flow meters and the inherent physical fluctuations in the flow conditions. Table 1 shows the measurement uncertainties for the instruments used in the current experiments. The last column denotes the maximum standard deviation as a percentage of the measured value observed in the current dataset of 71 flow conditions.

For each flow condition, the quantities were acquired at 500 Hz for 10 s to obtain time-averaged values after reaching a steady state. The resulting maximum uncertainties in the measurement of gas and liquid flow rates are found to be 2.5% and 1% of the measured values, respectively.

3. Results and discussion

The void fraction measurements were performed under 71 different flow conditions. Each flow condition was characterized by the velocity inlet boundary conditions, namely, volumetric flux of gas $\langle j_g \rangle$ and volumetric flux of liquid $\langle j_f \rangle$. The range of flow conditions covered in this study are $0.13\,\text{m/s} < \langle j_g \rangle < 2.65\,\text{m/s}$ and $0.8\,\text{m/s} < \langle j_f \rangle < 5.1\,\text{m/s}$. The test matrix is presented using coordinates of volumetric flux of gas and liquid flow as shown in Figure 5.

3.1 Flow visualization

The flow visualization study reveals the flow regimes observed under the current set of test conditions. Figure 6 shows the images obtained using the high-speed video camera in various flow regimes. The images presented are as acquired by the camera without any morphological transformation. The void fraction reported in each panel is the time-averaged value of the volume-averaged void fraction calculated using the image processing algorithm. The time series of the volume-averaged void fractions corresponding to these flow conditions are presented in Figure 7.

3.2 Calibration of impedance meter

The present measurement method determines the current passing through the test cell for a given potential difference at a known excitation frequency. Thus, the measured current is proportional to the admittance, *i.e.*, the inverse of the impedance of the two-phase mixture in the test cell. Further, in order to make the measurement independent of the material properties, the measured admittance is normalized as: :

$$G^* = \frac{G_m - G_1}{G_0 - G_1}, \tag{1}$$

where G_m is the instantaneous two-phase mixture admittance, G_0 is the admittance with zero void fraction (i.e., for single-phase liquid) and G_1 is the admittance when the void fraction is unity (i.e., for single-phase gas). Finally, the liquid fraction is a monotonically increasing function of normalized admittance, G^*. Hence the void fraction is proportional to $\alpha_{imp} = 1 - G^*$. For finely dispersed bubbly flow (void fraction < 10%), the functional relationship can be obtained by the effective conductivity of a medium impregnated with uniformly distributed non-conducting spheres. The expression for the effective conductivity given by Maxwell (1873) to a first-order approximation is

$$G^* = 1 - \frac{3\alpha}{2 + \alpha}, \tag{2}$$

where α is the void fraction of the dispersed phase. This model is applicable to the bubbly flow regime for void fractions less than 0.2. For void fractions above this limit, the sensor must be calibrated due to the statistical nature of the distribution of voids, where no closed-form analytical solution is available. The impedance meter is calibrated in a time-averaged sense. That is, the time-averaged value of the impedance meter reading $\langle \alpha_{imp} \rangle_t$ is compared with the time-averaged void fraction $\langle \alpha \rangle_{V,t,im}$ obtained by flow visualization.

Figure 7 shows the calibration curve of the impedance meter against the void fraction obtained by image processing for various flow regimes. The data show that the instrument has a nearly linear response. The data are also compared with eq. (2) for bubbly flow conditions. It can be observed that the data match the predicted values from this equation closely for void

fractions less than 0.15. A third-order polynomial curve is fit to the data to obtain a calibration curve. The calibration curve is given by

$$\alpha_{cal} = -1.18\alpha_{imp}^3 + 1.57\alpha_{imp}^2 + 0.61\alpha_{imp} . \tag{3}$$

In order to assess the accuracy of the measurement, mean square deviation is calculated as

$$E_{RMS} = \sqrt{\frac{1}{N}\sum_{i=1}^{N}\left(\alpha_{cal} - \langle\alpha\rangle_{V,t,im}\right)^2} \tag{4}$$

where, α_{cal} and $\langle\alpha\rangle_{V,t,im}$ are void fractions obtained from the calibration curve and by image processing, respectively. The mean square deviation is 0.023.

In order to validate the measurement of void fraction by the impedance meter, the void fraction measured by the impedance meter is plotted against the ratio of gas volumetric flux to total volumetric flux, β, which is defined as,

$$\beta = \frac{\langle j_g \rangle}{\langle j_g \rangle + \langle j_f \rangle} . \tag{5}$$

In the case of the homogeneous flow model, i.e. under the assumptions of uniform distribution phases in flow cross-section and equal velocities, the void fraction is given by

$$\alpha = \beta . \tag{6}$$

In view of the drift flux model, the relation between void fraction and volumetric fluxes is given by Zuber and Findlay (1965),

$$\langle\alpha\rangle = \frac{\langle j_g \rangle}{C_0\left(\langle j_g \rangle + \langle j_f \rangle\right) + \langle\langle v_{gj} \rangle\rangle} . \tag{7}$$

In eq. (7), C_0 is the distribution parameter, while $\langle\langle v_{gj} \rangle\rangle$ is the void-weighted drift velocity. These two parameters are specified by empirical correlations. The recommended value for the

distribution parameter is 1.2 as suggested by Armand (1946), Ali et al. (1993) and Mishima and Hibiki (1996). For horizontal flow, the drift velocity is close to zero. Figure 8 shows a comparison of the measured void fraction against the homogeneous flow and drift-flux models. The agreement between the predictions from both models and the data is remarkable considering the lack of established values for parameters in the drift flux model for the case of microchannel flow. Since the void fraction is a function of flow boundary conditions, i.e., volumetric fluxes of gas and liquid, the measured void fraction contours are plotted on gas and liquid volumetric flux coordinates in Figure 9. Such contour maps are helpful in developing void fraction correlations for microchannel two-phase flows.

3.3 Flow regime identification

The approach originally developed by Jones and Zuber (1975), which utilizes the probability density functions (PDF) of the void fraction fluctuations as flow regime indicators, is employed for flow regime identification. Physically, the PDF denotes the contribution of different kinds of bubbles to the time-averaged void fraction for a given flow condition. The normalized time series signal obtained by the impedance meter, $G^*(t)$, is used for this purpose. The PDF of $G^*(t)$ denoted by $f_{G^*}(G^*)$ is calculated using the kernel smoothing density estimation method described by Bowman and Azzalini (1997). A normal kernel is used as the smoothing function. The PDF $f_{G^*}(G^*)$ is evaluated at 200 discrete points in the domain of $G^* \in [0,1]$. Thus, each flow condition is represented by a 200-dimensional vector. The problem of identifying flow regimes is equivalent to identifying clusters of vectors in 200-dimensional vector space. The clusters of vectors are found by minimizing the distance between the vectors representing flow conditions and the weight vectors corresponding to a flow regime. After minimization, the weight vector positions align with the centroid of the clusters. Thus, the weight vectors that

denote the positions of the cluster centroids are characteristic of the flow regime. This optimization problem is solved by the *Kohonen Self-Organizing Map* algorithm for pattern recognition implemented in the Neural Network Toolbox of MATLAB based on the method developed by Kohonen (1997). Physical interpretation of the recognized patterns is accomplished by comparing them with the flow regimes observed using the high-speed camera.

Figures 10 to 14 show examples of the impedance meter signals and the corresponding PDFs obtained for various air-water flow regimes. The flow regimes, their qualitative description and characteristics of the corresponding impedance meter signals are as follows. It is noted that stable annular flow could not be achieved with the current experimental setup.

- Bubbly Flow: Bubbly flow is characterized by spherical or ellipsoidal bubbles dispersed in the continuous phase. The major diameters of these bubbles are smaller than the width of the channel. The PDF $f_{G^*}(G^*)$ shows a relatively small width and a peak at higher admittance (Fig. 10).
- Cap-Bubbly Flow: As the bubble size increases, it is confined by the channel walls. It is distorted and forms a cap-shaped bubble with a round nose at its downstream end. The PDF is characterized by two distinct peaks located close to each other (Fig 11). The peak corresponding to higher G^* represents the liquid regions between the bubbles, while that corresponding to lower G^* represents cap bubbles.
- Slug Flow: Long bullet-shaped bubbles are separated by liquid or small spherical bubbles. The PDF shows two distinct peaks, with one located at low G^* corresponding to slug bubbles and the other located at high G^* corresponding to the continuous liquid phase between the slug bubbles (Fig. 12).

- Churn-turbulent Flow: Due to turbulent agitation at the higher flow rates, churn-turbulent flow exhibits interacting slug bubbles with distorted shape. This leads to a wider spread in the PDF, where peaks corresponding to slug bubbles and liquid gaps between them are merged. It should be noted here that the existence of a churn-turbulent regime does not imply higher void fraction than that in the slug flow regime in a time-averaged sense (Fig. 13).
- Long Slug Flow: This regime is characterized by the occurrence of long stable slugs such that it appears to have a structure similar to annular flow in a local or short-time-averaged sense. The PDF shows a high peak at low G^*. Annular flow was not observed in the current dataset (Fig. 14).

Using the quantitative method of flow regime classification described above, the dataset was categorized into five regimes. The result of this classification is shown in Figure 15. The flow conditions are presented on coordinates of volumetric flux of the gas and liquid phases. The contours of time-averaged void fraction are superimposed on the flow regime map. This shows the relationship between flow regime boundaries and the void fraction. This map could be used for the development of theoretical flow regime transition criteria in microchannel two-phase flow.

4. Summary and conclusions

Void fraction is measured in air-water two-phase flow in a microchannel of cross-section 780 μm X 780 μm using a custom-designed impedance void meter. The impedance void meter is calibrated against the time-averaged void fraction determined from flow visualization using a high-speed movie camera. The calculated time-averaged void fraction shows reasonable

agreement with those predicted by the homogeneous flow and drift flux models. However, a conclusive statement in favor of a particular model cannot be made since the model parameters (e.g., the distribution parameter and the drift velocity for the drift-flux model) are not available for microchannel flows.

The probability density function (PDF) of the time series signal obtained by the impedance meter is utilized for quantitative characterization of two-phase flow regimes. The flow regimes are identified using a Kohonen Self-organizing map. The present study shows that the impedance void meter designed in this work can be used for microchannel two-phase flows for the measurement of void fraction and identification of flow regimes. The void fraction and flow regime data obtained by the impedance void meter may be used for developing and benchmarking theoretical flow regime transition criteria for microchannel two-phase flows.

Further studies are in progress for extending the flow regime map to include annular flow, in addition to developing flow regime maps for additional flow channel geometries. The measurement technique developed here can be used to study non-adiabatic and boiling flows with similar geometry of electrodes along with the same electronic circuit, as long as the changes in electrical properties of the fluid with temperature are taken into account.

Acknowledgments

This work was funded by the Office of Naval Research (Grant No. N000141010921). The authors are grateful to Dr. Mark Spector for his support.

References

Ali, M.I., Sadatomi, M., Kawaji, M., 1993. Two-phase flow in narrow channels between flat plates. Canadian Journal of Chemical Engineering 71, 657–666.

Andreussi, P., Di Donfrancesco, A., and Messia, M., 1988. An impedance method for the measurement of liquid hold up in two-phase flow. Int. J. Multiphase Flow 14, 777-785.

Armand, A.A., 1946. The resistance during the movement of a two-phase system in horizontal pipes. Izv. Vses. Teplotekh., Inst. 1, (AERE-Lib/Trans 828), 16–23.

Asali, J. C., Hanrtatty, T. J. and Andreussi, P., 1985. Interficial drag and film height in vertical annular flow. AIChE J. 31, 895-902.

Bertsch, S.S., Groll, E.A. and Garimella, S.V., 2008. Review and comparative analysis of studies on saturated flow boiling in small channels. Nanoscale MicroscaleThermophys. Eng. 12, 187–227.

Bowman, A. W., and A. Azzalini, Applied Smoothing Techniques for Data Analysis, New York: Oxford University Press, 1997.

Coney, M.W.E., 1973. The theory and application of conductance probes for the measurement of liquid film thickness in two-phase flow. Journal of Physics E (Scientific Instruments) 6, 903-911.

Costigan, G. and Whalley, P. B., 1997. Slug flow regime identification from dynamic void fraction measurements in vertical air-water flows. Int. J. Multiphase Flow 23, 263–282.

Fossa, M., 1998. Design and performance of a conductance probe for measuring the liquid fraction in two-phase gas-liquid flows. J. Flow Meas. Instrum. 9, 103-109.

Garimella, S. V. and Sobhan, C. B., 2003. Transport in microchannles – a critical review. Annu. Rev. Heat Transfer 13, 1-50.

Harirchian, T. and Garimella, S.V., 2008. Microchannel size effects on local flow boiling heat transfer to a dielectric fluid. Int. J. Heat Mass Transfer 51, 3724–3735.

Harirchian, T., and Garimella, S.V., 2009. Effects of channel dimension, heat flux and mass flux on flow boiling regimes in microchannels. Int. J. Multiphase Flow 35, 349-362.

Harirchian, T. and Garimella, S. V., 2010. A comprehensive flow regime map for microchannel flow boiling with quantitative transition criteria. Int. J. Heat Mass Transfer 53, 2694-2702.

Hewitt, G. F., 1983. Two-Phase flow and its applications: past, present and future. Heat Transfer Engineering 4, 67-79.

Jones Jr. O.C. and Zuber N., 1975. The interrelation between void fraction fluctuations and flow patterns in two-phase flow. Int. J. Multiphase Flow 2, 273-306.

Julia, J. E., Liu, Y., Paranjape, S. and Ishii, M., 2008. Local flow regimes analysis in vertical upward two-phase flow. Nucl. Eng. and Design 238, 156-169.

Kawahara, A., Sadatomi, M., Kumagae, K., 2006. Effects of gas–liquid inlet/mixing conditions on two-phase flow in microchannels. Progress in Multiphase Flow Research 1, 197–203.

Kawahara, A., Sadatomi, M., Nei, K. and Matsuo, H., 2009. Experimental study on bubble velocity, void fraction and pressure drop for gas–liquid two-phase flow in a circular microchannel. International Journal of Heat and Fluid Flow 30, 831–841.

Kawaji, M., Kawahara, A., Mori, K., Sadatomi M., Kumagae, K., 2006. Gas–liquid twophase flow in microchannels: the effects of gas–liquid injection methods. In: Proceedings of the 18th National and Seventh ISHMT–ASME Heat Transfer.

Kohonen, T., Self-Organizing Maps, Second Edition, Berlin: Springer-Verlag, 1997.

Matsui, G., 1984. Identification of flow regimes in vertical gas-liquid two-phase flow using differential pressure fluctuations. Int. J. Multiphase Flow 10, 711-720.

Maxwell, J. C. 1873, A Treatise on Electricity and Magnetism,3rd ed., Clarendon Press, Oxford, England.

Mi, Y., Ishii, M. and Tsoukalas, L. H., 1998. Vertical two-phase flow identification using advanced instrumentation and neural networks. Nucl. Eng. and Design 184, 409-420.

Mishima, K., Hibiki, T., 1996. Some characteristics of air–water two-phase flow in small diameter vertical tubes. Int. J. Multiphase Flow 22, 703–712.

Serizawa, A., Feng, Z., Kawara, Z., 2002. Two-phase flow in microchannels. Experimental Thermal and Fluid Science 26, 703–714.

Sobhan, C.B., and Garimella, S.V., 2001. A comparative analysis of studies on heat transfer and fluid flow in microchannels. Microscale Thermophys. Eng. 5, 293–311.

Soille, P. 2003, Morphological Image Processing, 2nd ed., Springer-Verlag, Germany.

The Mathworks Inc., 2009. MATLAB version 2009b

Tsochatzidis, N. A., Karapantios, T. D., Kostoglou, M. V., and Karabelas, A. J., 1992. A conductance method for measuring liquid fraction in pipes and packed beds. Int. J. Multiphase Flow 5, 653-667.

Tumanski, S. 2006, Principles of electrical measurement, CRC Press, Taylor & Francis, USA.

Tutu, N. K., 1982. Pressure fluctuations and flow pattern recognition in vertical two phase gas-liquid flows. Int. J. Multiphase Flow 8, 443-447.

Zuber, N. and Findlay, J. A., 1965. Average volumetric concentration in two-phase flow systems. J. Heat Transfer 87, 453-468.

List of Table and Figure Captions

Table 1. Measurement uncertainties as a percentage of measured value.

Fig 1. Impedance meter test cell. (a) Top view of test cell. (b) Base plate with flow channel and electrodes.

Fig 2. Air-water two-phase flow loop.

Fig 3. Impedance meter circuit. (a) Signal processing scheme. (b) Basic electronic circuit.

Fig 4. Image processing steps. (a) Original image, top view.. (b) Step 1, Rotated and cropped image for interrogation window. (c) Step 2, Background subtracted and threshold adjusted image. (d) Step 3, Edge detection. (e) Step 4, Remove interior boundaries. (f) Step 5, Edges after finding convex hull, superimposed on original image.

Fig 5. Test Matrix.

Fig. 6. Flow visualization and void fraction measured by image processing. Flow direction is from left to right. (a) Bubbly, $\langle j_g \rangle$ = 0.29 m/s, $\langle j_f \rangle$ = 0.83 m/s, $\langle \alpha \rangle_{V,t}$ = 0.20. (b) Cap Bubbly, $\langle j_g \rangle$ = 0.56 m/s, $\langle j_f \rangle$ = 0.83 m/s, $\langle \alpha \rangle_{V,t}$ = 0.37. (c) Slug, $\langle j_g \rangle$ = 1.39 m/s, $\langle j_f \rangle$ = 0.83 m/s, $\langle \alpha \rangle_{V,t}$ = 0.58. (d) Churn-Turbulent $\langle j_g \rangle$ = 2.26 m/s, $\langle j_f \rangle$ = 4.08 m/s, $\langle \alpha \rangle_{V,t}$ = 0.36. (e) Long Slug, $\langle j_g \rangle$ = 2.65 m/s, $\langle j_f \rangle$ = 0.82 m/s, $\langle \alpha \rangle_{V,t}$ = 0.65.

Fig. 7. Impedance meter calibration.

Fig. 8. Comparison of measured void fraction with homogeneous flow and drift-flux

models.

Fig. 9. Contours of void fraction.

Fig. 10. Impedance meter signal and its PDF for Bubbly flow, $\langle j_g \rangle$ = 0.29 m/s, $\langle j_f \rangle$ = 0.83 m/s, $\langle \alpha \rangle_{V,t}$ = 0.20.

Fig. 11. Impedance meter signal and its PDF for Cap-Bubbly, $\langle j_g \rangle$ = 0.56 m/s, $\langle j_f \rangle$ = 0.83 m/s, $\langle \alpha \rangle_{V,t}$ = 0.37.

Fig. 12. Impedance meter signal and its PDF for Slug, $\langle j_g \rangle$ = 1.39 m/s, $\langle j_f \rangle$ = 0.83 m/s, $\langle \alpha \rangle_{V,t}$ = 0.58.

Fig. 13. Impedance meter signal and its PDF for Churn Turbulent flow, $\langle j_g \rangle$ = 2.26 m/s, $\langle j_f \rangle$ = 4.08 m/s, $\langle \alpha \rangle_{V,t}$ = 0.36.

Fig. 14. Impedance meter signal and its PDF for Long Slug, $\langle j_g \rangle$ = 2.65 m/s, $\langle j_f \rangle$ = 0.82 m/s, $\langle \alpha \rangle_{V,t}$ = 0.65.

Fig. 15. Flow regime map obtained using impedance void meter signals.

Table 1. Measurement uncertainties as a percentage of measured value.

Instrument	Reported Measurement Accuracy	Maximum Standard Deviation
Liquid flow [ml/min]	0.2%	0.74%
Gas flow [ml/min]	0.1%	3.2 %
Pressure [kPa]	0.2%	2%
Temperature [K]	0.1%	0.05%

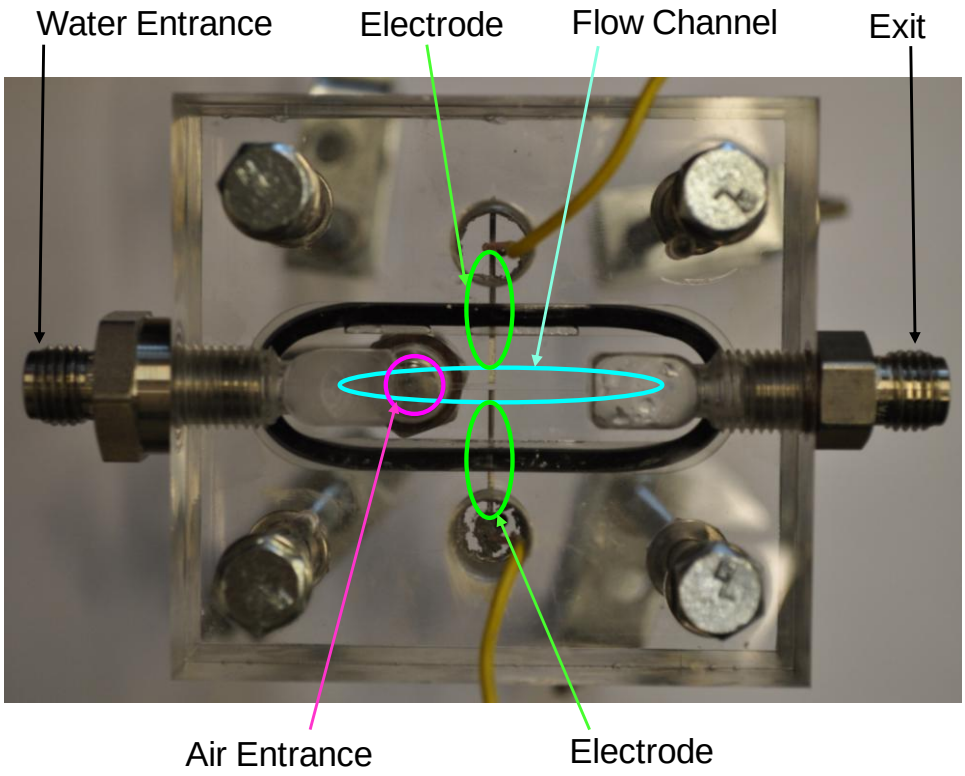

(a)

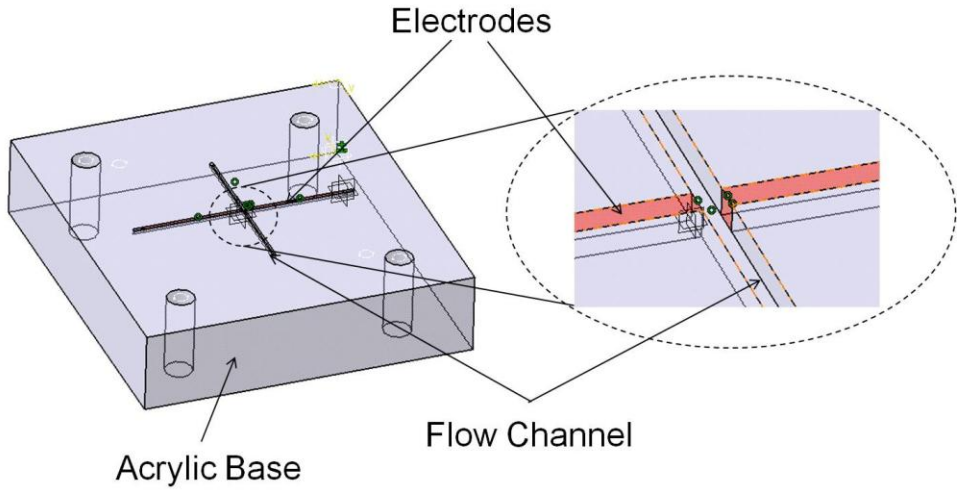

(b)

Figure 1. Impedance meter test cell: (a) top view, and (b) base plate with flow channel and electrodes.

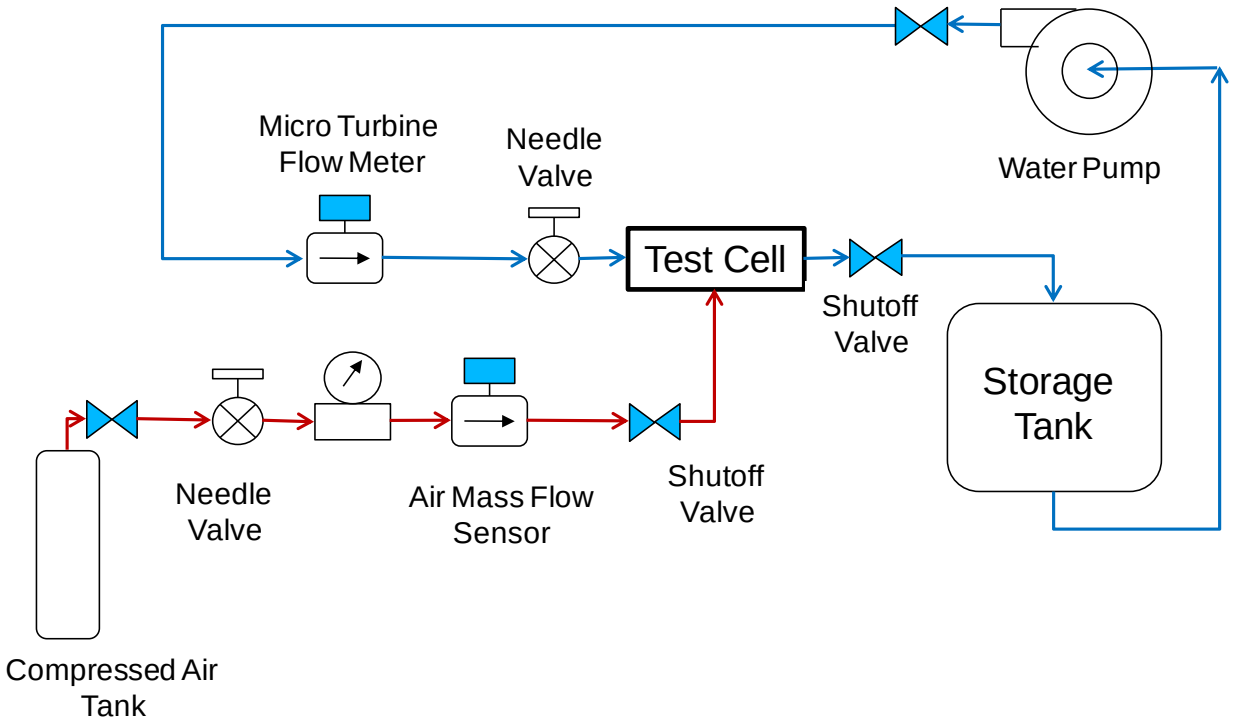

Figure 2. Air-water two-phase flow loop.

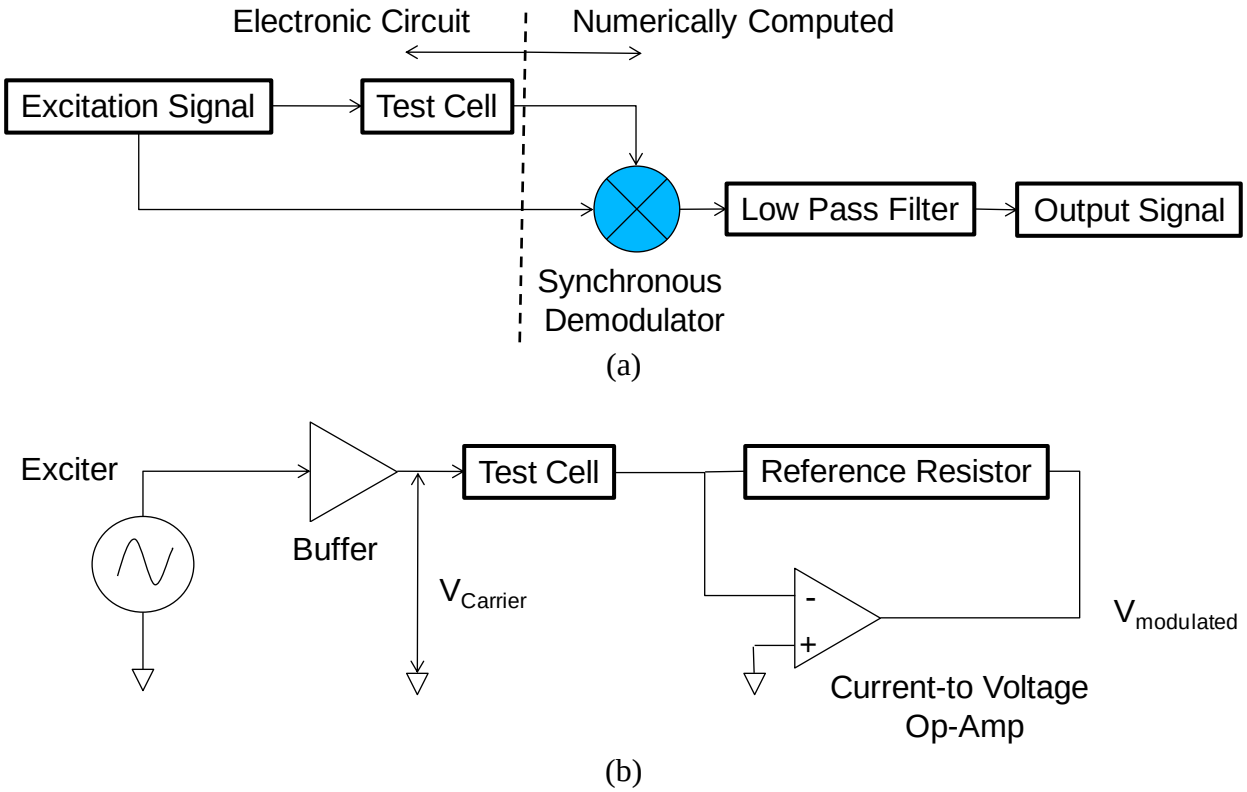

Figure 3. Impedance meter circuit: (a) signal-processing scheme, and (b) basic electronic circuit.

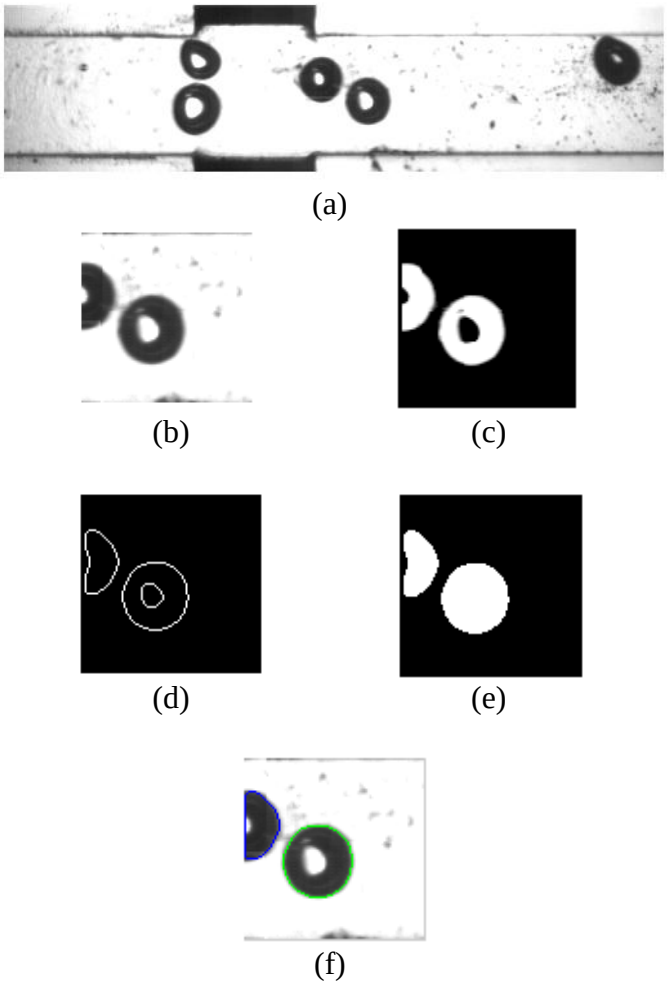

Figure 4. Image processing steps: (a) original image, top view; (b) Step 1, rotated and cropped image for interrogation window; (c) Step 2, background subtracted and threshold adjusted image; (d) Step 3, edge detection; (e) Step 4, remove interior boundaries; and (f) Step 5, edges after finding convex hull, superimposed on original image.

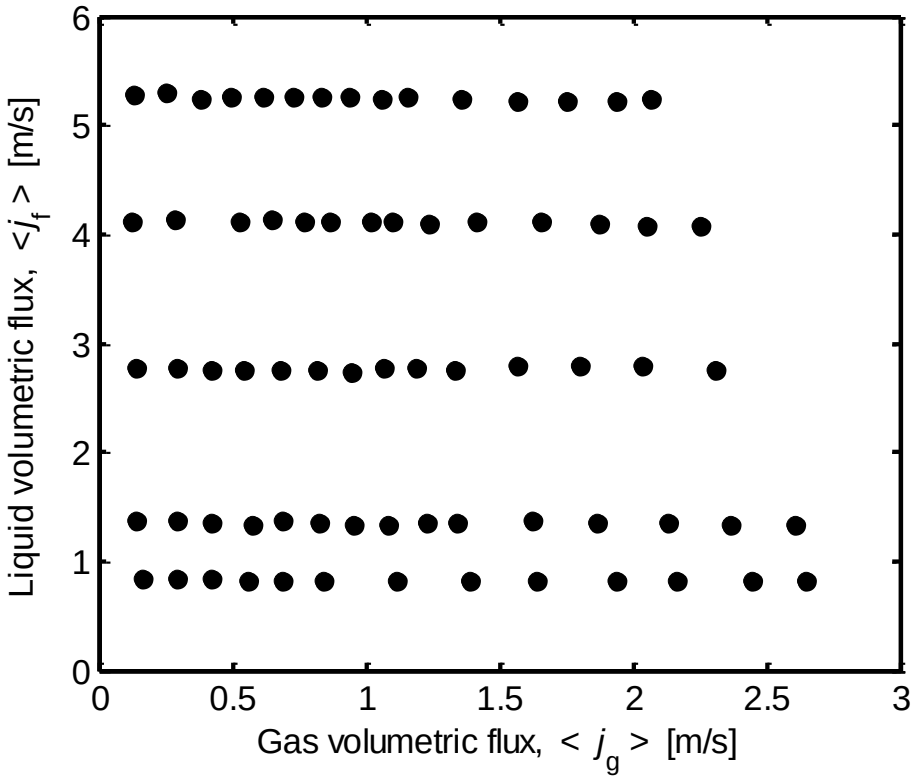

Figure 5. Test matrix.

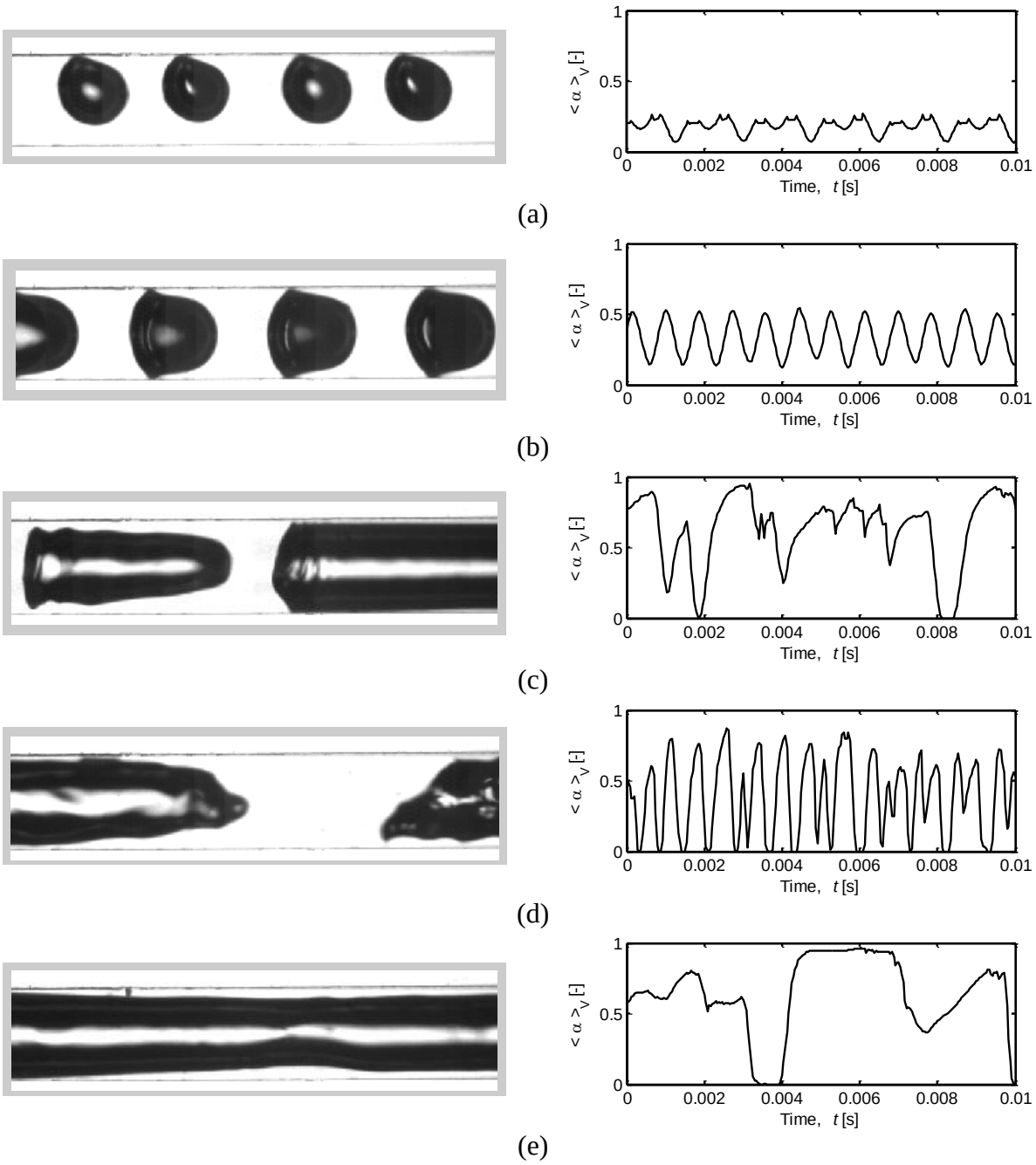

Figure 6. Flow visualization and void fraction measured by image processing. Flow direction is from left to right. (a) Bubbly, $\langle j_g \rangle$ = 0.29 m/s, $\langle j_f \rangle$ = 0.83 m/s, $\langle \alpha \rangle_{V,t}$ = 0.20. (b) Cap Bubbly, $\langle j_g \rangle$ = 0.56 m/s, $\langle j_f \rangle$ = 0.83 m/s, $\langle \alpha \rangle_{V,t}$ = 0.37. (c) Slug, $\langle j_g \rangle$ = 1.39 m/s, $\langle j_f \rangle$ = 0.83 m/s, $\langle \alpha \rangle_{V,t}$ = 0.58. (d) Churn-Turbulent $\langle j_g \rangle$ = 2.26 m/s, $\langle j_f \rangle$ = 4.08 m/s, $\langle \alpha \rangle_{V,t}$ = 0.36. (e) Long Slug, $\langle j_g \rangle$ = 2.65 m/s, $\langle j_f \rangle$ = 0.82 m/s, $\langle \alpha \rangle_{V,t}$ = 0.65.

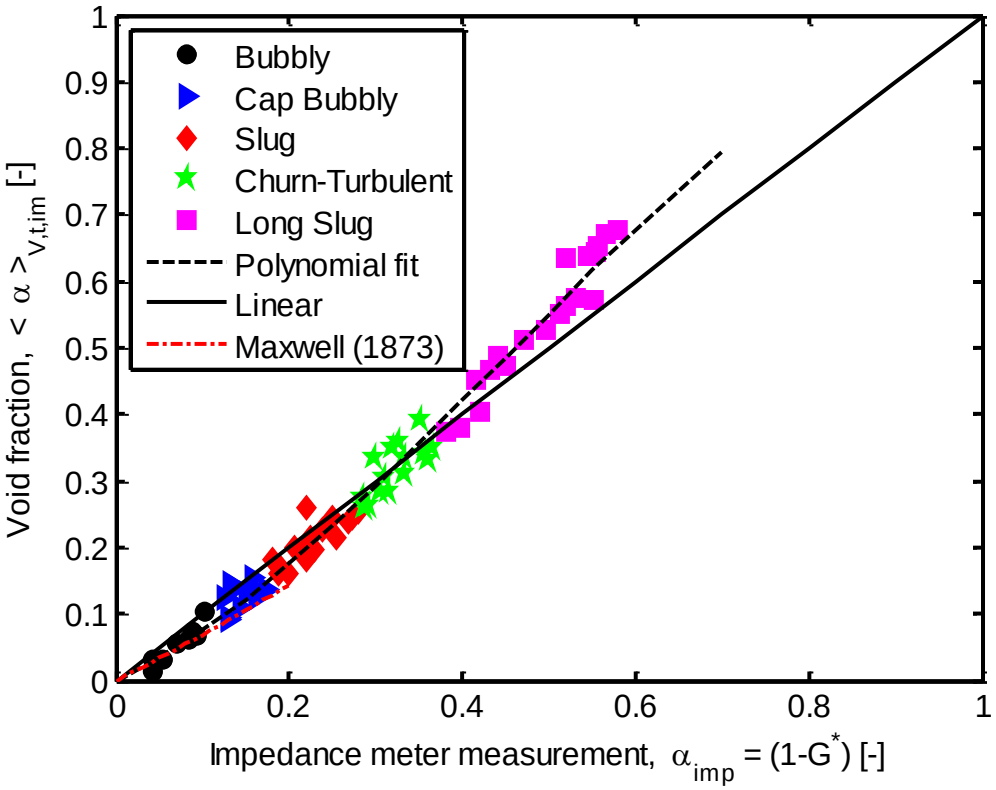

Figure 7. Impedance meter calibration.

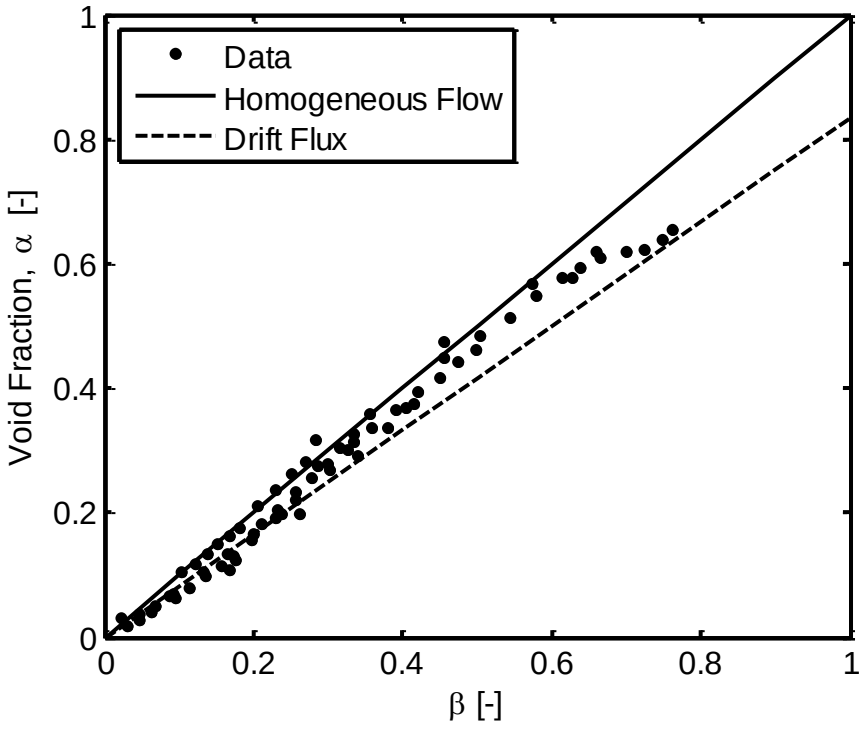

Figure 8. Comparison of measured void fraction with homogeneous flow and drift-flux models.

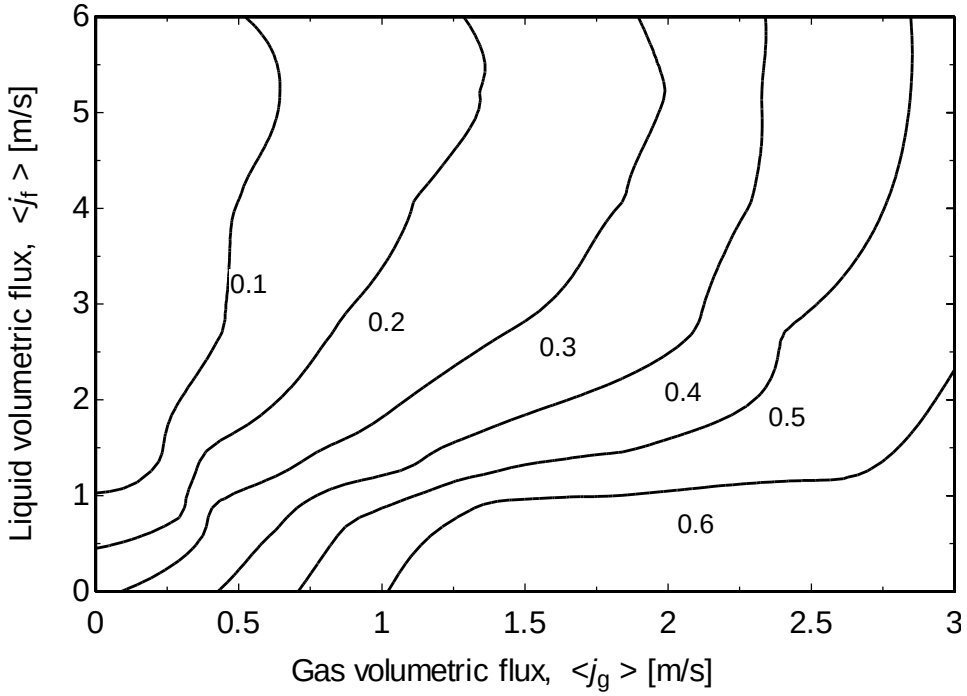

Figure 9. Contours of void fraction.

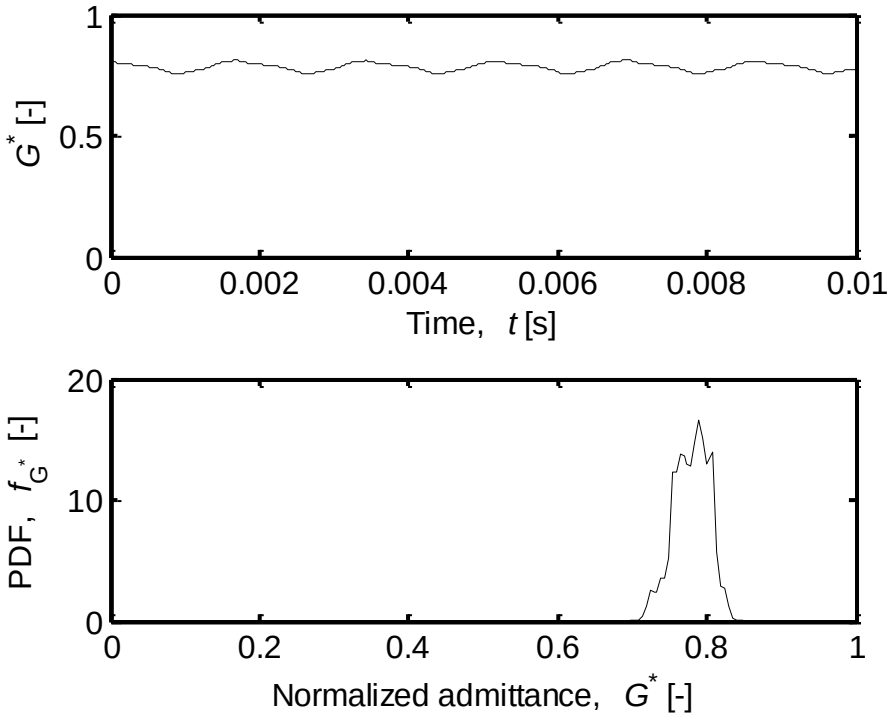

Figure 10. Impedance meter signal and its PDF for bubbly flow, $\langle j_g \rangle$ = 0.29 m/s, $\langle j_f \rangle$ = 0.83 m/s, $\langle \alpha \rangle_{V,t}$ = 0.20.

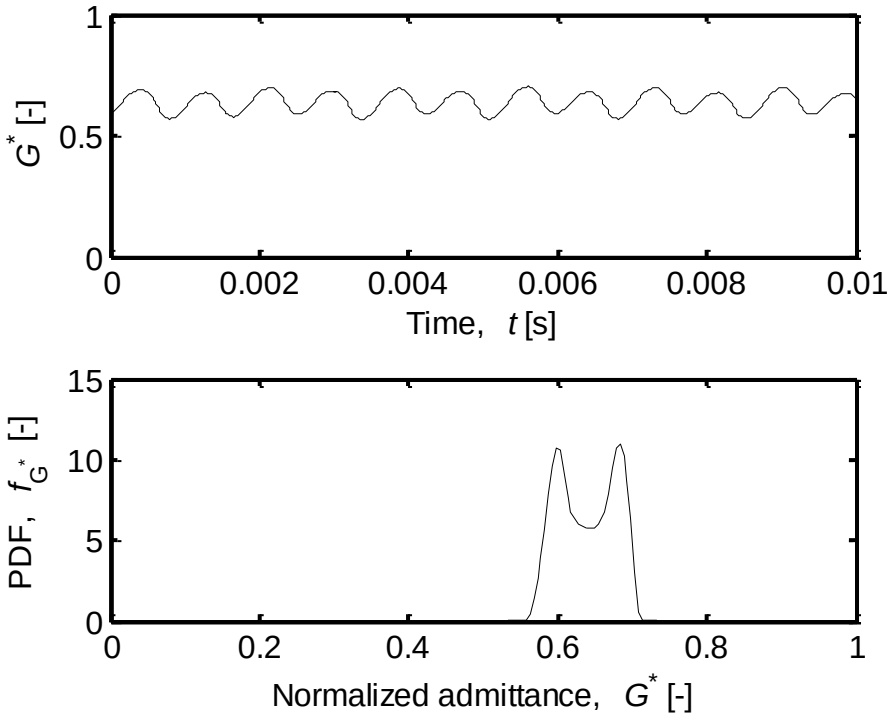

Figure 11. Impedance meter signal and its PDF for cap-bubbly flow, $\langle j_g \rangle$ = 0.56 m/s, $\langle j_f \rangle$ = 0.83 m/s, $\langle \alpha \rangle_{V,t}$ = 0.37.

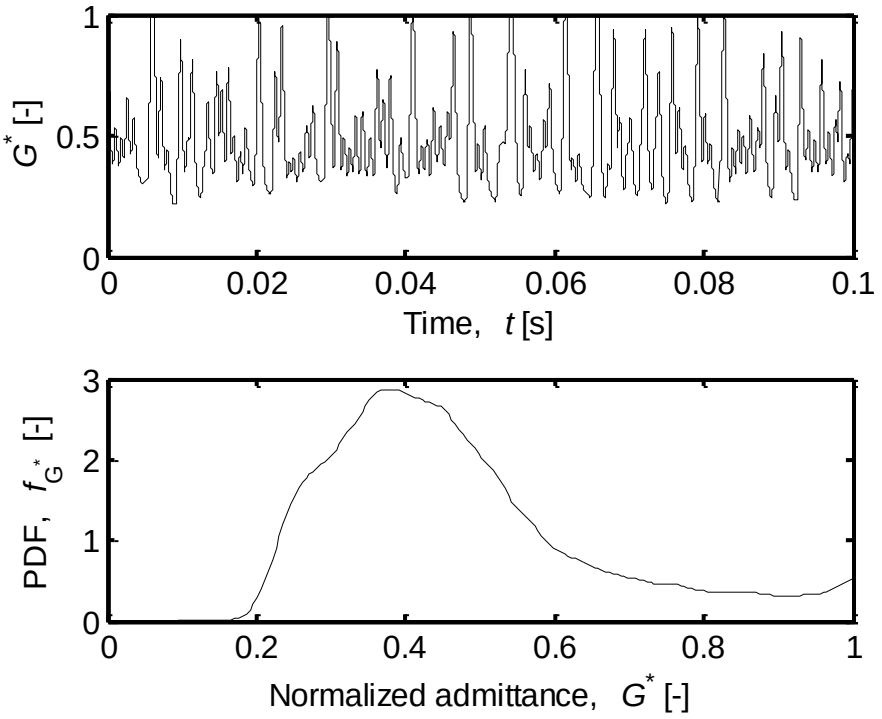

Figure 12. Impedance meter signal and its PDF for slug flow, $\langle j_g \rangle$ = 1.39 m/s, $\langle j_f \rangle$ = 0.83 m/s, $\langle \alpha \rangle_{V,t}$ = 0.58.

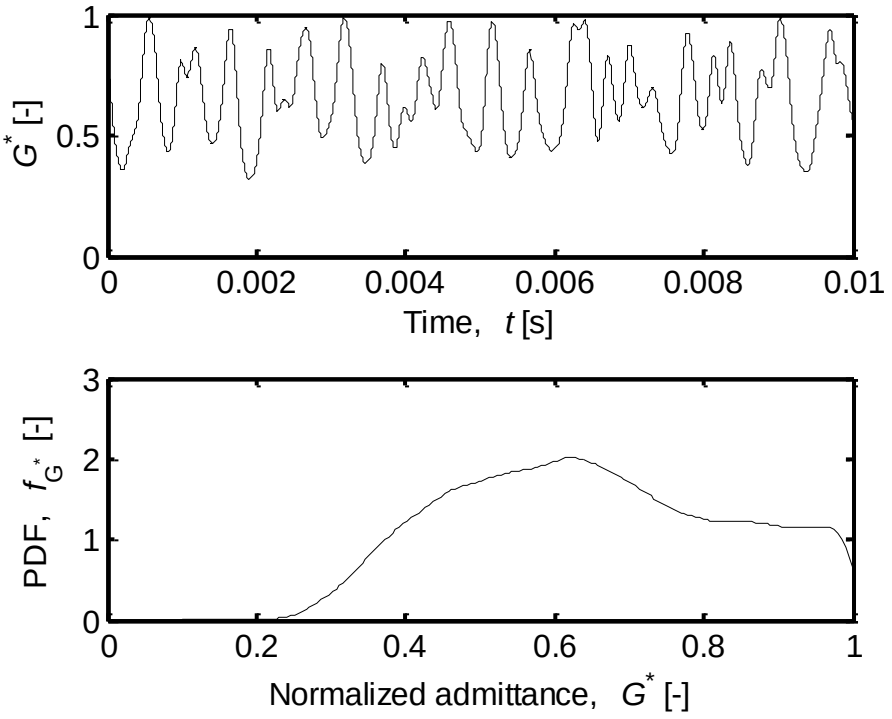

Figure 13. Impedance meter signal and its PDF for churn turbulent flow, $\langle j_g \rangle$ = 2.26 m/s, $\langle j_f \rangle$ = 4.08 m/s, $\langle \alpha \rangle_{V,t}$ = 0.36.

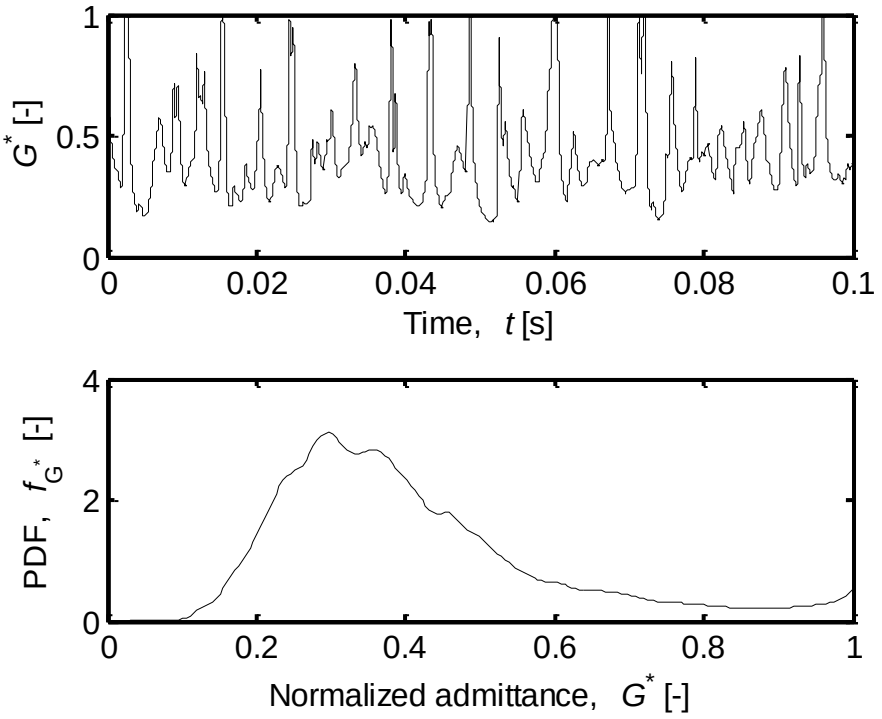

Figure 14. Impedance meter signal and its PDF for long slug flow, $\langle j_g \rangle$ = 2.65 m/s, $\langle j_f \rangle$ = 0.82 m/s, $\langle \alpha \rangle_{V,t}$ = 0.65.

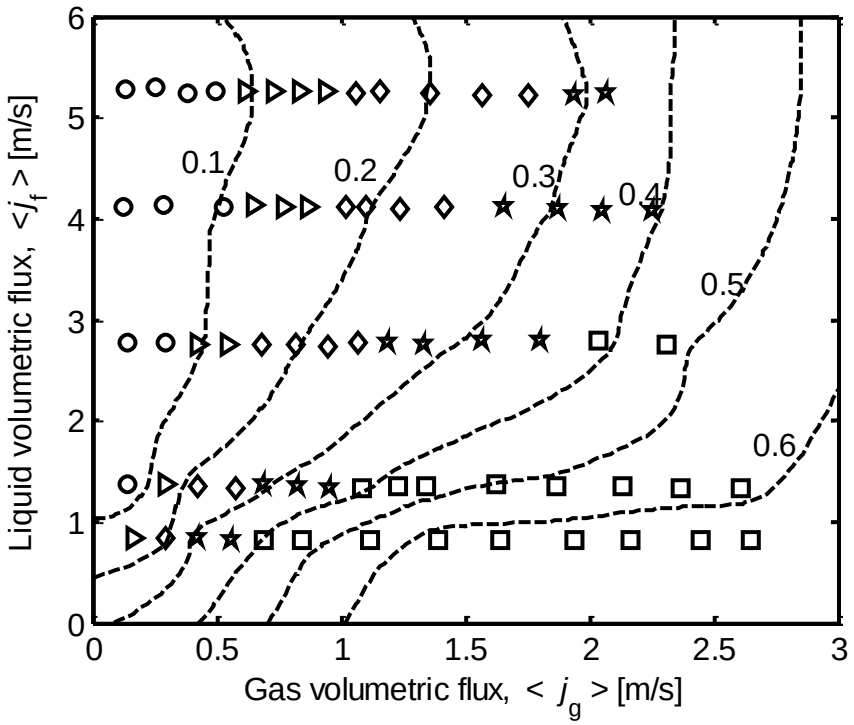

Legend: ○: Bubbly, ▷: Cap Bubbly, ◊: Slug,
☆: Churn-Turbulent, □: Long Slug,
Level Lines: Void fraction contours

Figure 15. Flow regime map obtained using impedance void meter signals.